Supporting Information

CNTs Support 2D NiMOF Nanosheets for Asymmetric Supercapacitors with High Energy Density

Nianxiang Hu[a,b], Jiang Liao[a,b], Xueliang Liu[c], Jinlong Wei[b], Xuanbing Wang[a,b], Li Wang[b], Min Li[b], Naixuan Zong[a,b], Ruidong Xu[a,b*], Linjing Yang[a,b*], Junli Wang[c*]

a State Key Laboratory of Complex Nonferrous Metal Resources Clean Utilization, Kunming University of Science and Technology, Kunming 650093, P. R. China
b Faculty of Metallurgical and Energy Engineering, Kunming University of Science and Technology, Kunming 650093, P. R. China
c Research Center for Analysis and Measurement, Kunming University of Science and Technology, Kunming 650093, P. R. China

* Corresponding author E-mail: rdxupaper@aliyun.com (R. Xu);
* Corresponding author E-mail: eslinjingyang@kust.edu.cn (L. Yang);
* Corresponding author E-mail: 20070141@kust.edu.cn (J. Wang).

The coulombic efficiency was calculated according to the following equation:[1]

$$\eta = \frac{t_d}{t_c} \times 100\% \qquad (1)$$

Where t_d was the discharge and t_c represented charge time.

The Calomel electrode is really not suitable for use in KOH solution directly due to large liquid junction potential. In fact, we used a salt bridge (Fig. S1b) to connect Calomel electrode and the electrolyte, so the potential difference between these two can be minimized and eliminated.[2]

Mechanism of salt bridge: A salt bridge is inserted between the two solutions to replace the original direct contact of the two solutions, reducing and stabilizing the junction potential (When two kinds of electrolytes with different compositions or activity are in contact, due to the different migration speeds of positive and negative ions diffusing through the interface, the positive and negative charges are separated, and an electric double layer is formed at the solution interface. Therefore, the potential difference, namely as liquid junction diffusion potential or liquid junction potential for short), is so as to minimize the liquid junction potential and nearly eliminate it.[3, 4]
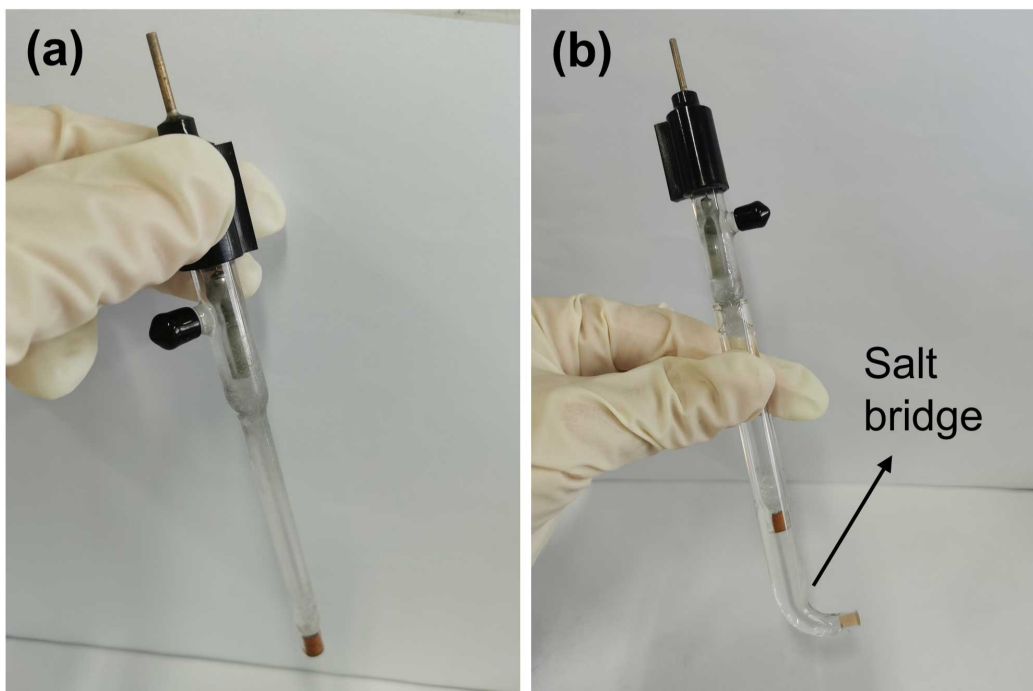
Fig. S1 (a) SCE reference electrode without salt bridge; (b) SCE reference electrode with salt bridge.

The function of the salt bridge: Due to the high concentration of the electrolyte in the salt bridge, the diffusion effect on the two new interfaces mainly comes from the salt bridge, stabilizing the liquid junction potential generated on the interfaces. Owing to the migration speeds of positive and negative ions in the salt bridge are almost the same, the two liquid junction potentials generated at the interface have opposite directions and almost equal values, so that the liquid junction potentials are minimized and nearly eliminated.[5]

The function of the external salt bridge solution: (1) Prevent the inner salt bridge solution of the reference electrode from leaking into the test solution from the liquid junction to interfere with the measurement; (2) Prevent the harmful ions in the test solution from diffusing into the inner salt bridge solution of the reference electrode to affect its electrode potential.
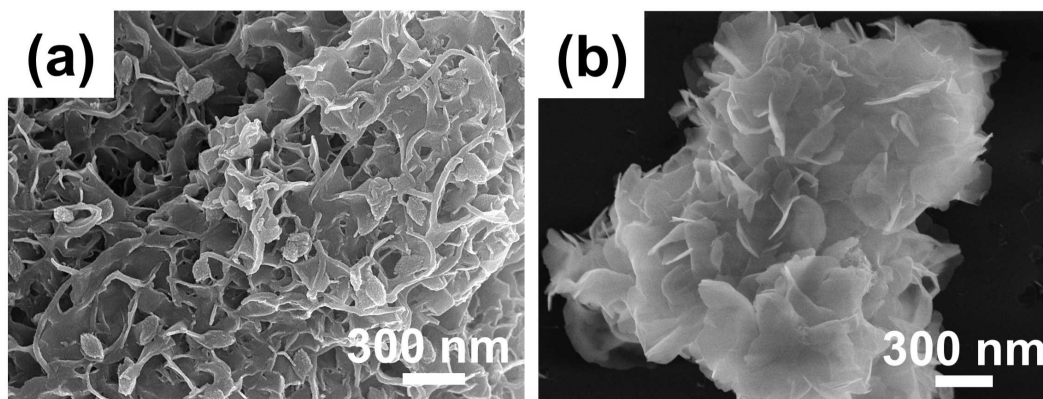
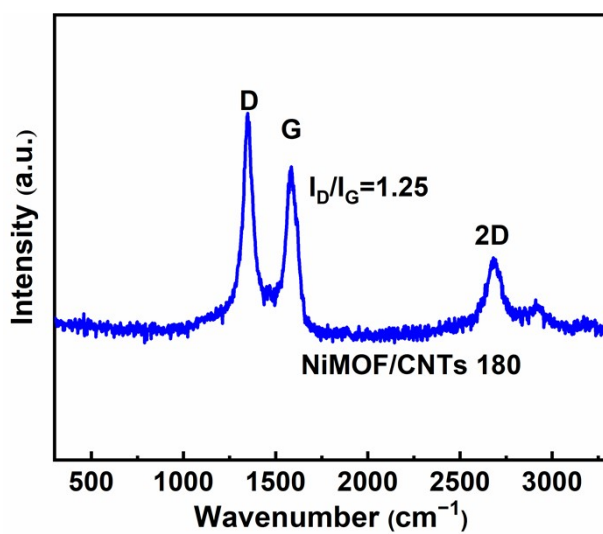**Fig. S2.** (a) SEM images of NiMOF/CNTs 170 and (b) SEM images of NiMOF/CNTs 190.
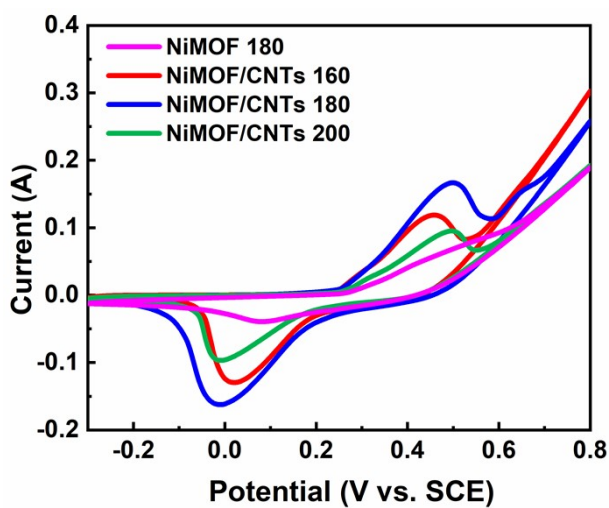

Fig. S3. Raman spectrum of NiMOF/CNTs 180.

Fig. S4. The CV curves of different electrodes at 20 mV s^{-1}.

The SEM images of NiMOF/CNTs 180 with different mass contents (1%, 2%, 5%, 10%, 15%) of the CNTs were shown in Fig. S5. As we can see, the NiMOF nanosheets exhibited slight agglomeration with a mass contents of 1%, which indicated that there were not enough CNTs as skeleton for their growth. On the contrary, the NiMOF nanosheets were encapsulated when the CNTs were contained in excess ($\geq$15%), implying that the contents of the CNTs should be appropriate.
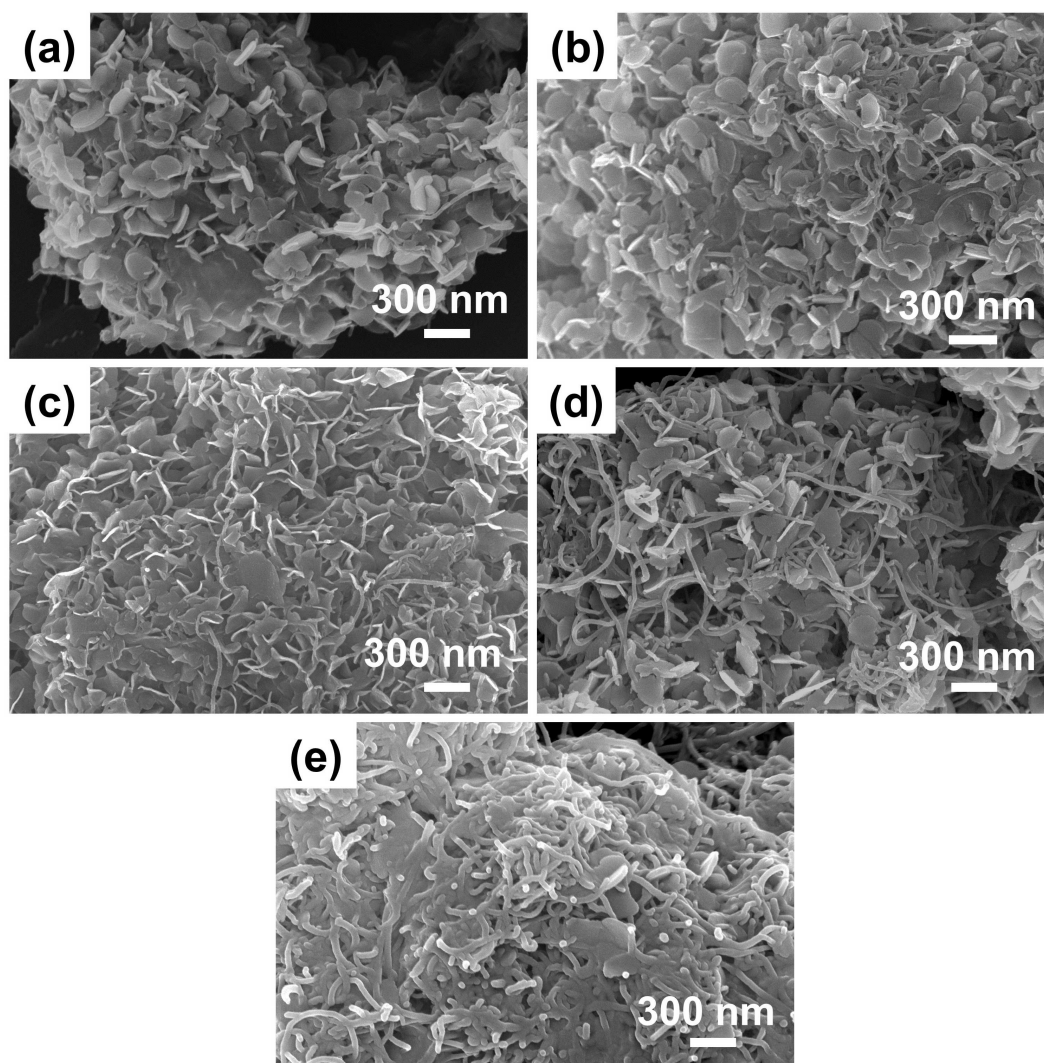

Fig. S5 SEM images of NiMOF/CNTs 180 electrode materials with different mass contents of the CNTs, (a) 1%; (b) 2%; (c) 5%; (d) 10%, and (e) 15%.

As in Fig. S6a, with the increasing contents of the CNTs, the conductivity of NiMOF/CNTs 180 electrode materials improved. When the CNTs content were 1%, 2%, 5%, 10% and 15%, the corresponding electrode materials possessed the conductivity of 0.6 S cm^{-1}, 4.7 S cm^{-1}, 11.8 S cm^{-1}, 18.2 S cm^{-1} and 25.8 S cm^{-1}, respectively. In conclusion, the introduction of the CNTs can enhance the conductivity

of the electrode materials, thus accelerating the transport of electrons and ions and promoting the occurrence of the redox reactions;[6, 7] (Conductivity)
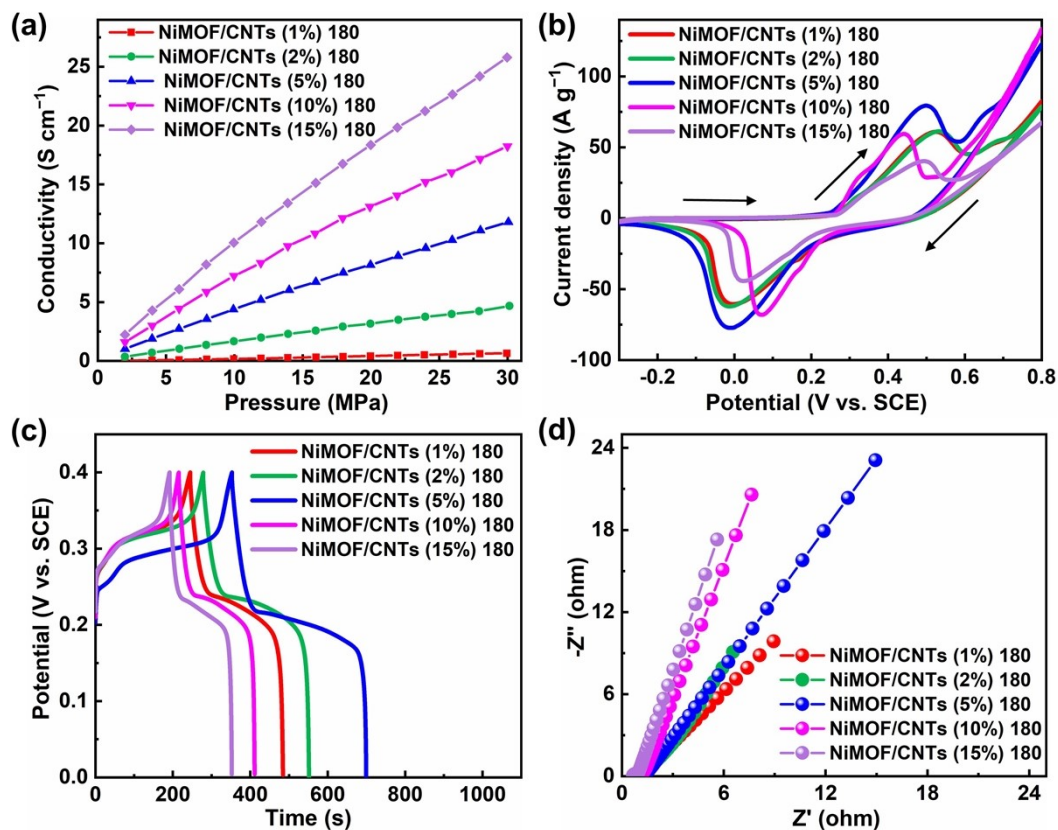

Fig. S6 (a) CV curves of electrode materials with different CNTs contents at 20 mV s^{-1}. (b) GCD curves of electrode materials with different CNTs contents at 2 A g^{-1}. (c) Nyquist diagram of electrode materials with different CNTs contents and (d) Conductivity of electrode materials with different CNTs contents.

As in Fig. S6b, the CV curves of NiMOF/CNTs 180 electrode materials with different CNTs contents exhibited distinct redox peaks, in which NiMOF/CNTs (5%) 180 presented the largest area of CV curves and NiMOF/CNTs (15%) 180 presented the smallest. It was consistent with the result in GCD curves (Fig. S6c) that the discharging time of NiMOF/CNTs (5%) 180 exhibited the longest, suggesting that the highest specific capacitance of NiMOF/CNTs 180 was obtained when the contents of CNTs keep at 5%. With the contents of the CNTs increased or decreased, the discharging time reduced. According to the discharge time, the NiMOF/CNTs 180 electrode materials with the CNTs contents of 1%, 2%, 5%, 10% and 15% demonstrated specific capacitance of 1200.0 F g^{-1}, 1333.5 F g^{-1}, 1855.0 F g^{-1}, 982.5 F g^{-1} and 808.0 F g^{-1}, respectively. Therefore, the introduction of appropriate contents of the CNTs boosted

the specific capacitance of these electrode materials, because NiMOF nanosheets played a major role in energy storage. In addition, these electrode materials exhibited small Rct (Fig. S6d) of 0.39 Ω, 0.38 Ω, 0.32 Ω, 0.40 Ω and 0.44 Ω, respectively, indicating a well interfacial charge transfer existed between the electrolyte and the electrodes. (Electrochemical performances)
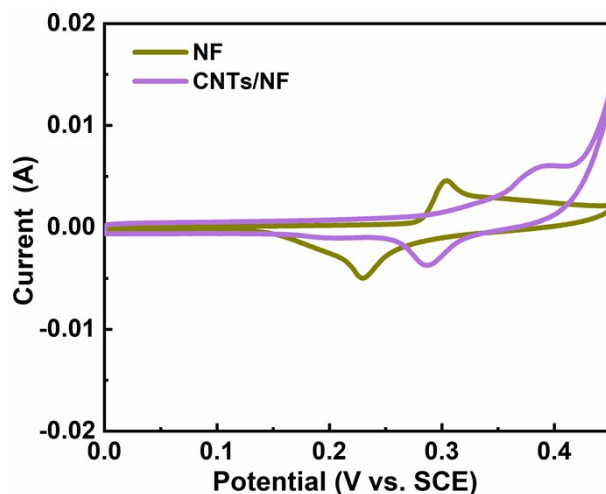

Fig. S7. The CV curves of different electrodes at 20 mV s⁻¹.

As shown in Fig. S7, the CV curves of NF and CNTs/NF significantly displayed a smaller area and potential than that of NiMOF/CNTs, illustrating that only the complex of NiMOF and CNTs dominate the pseudocapacitive.
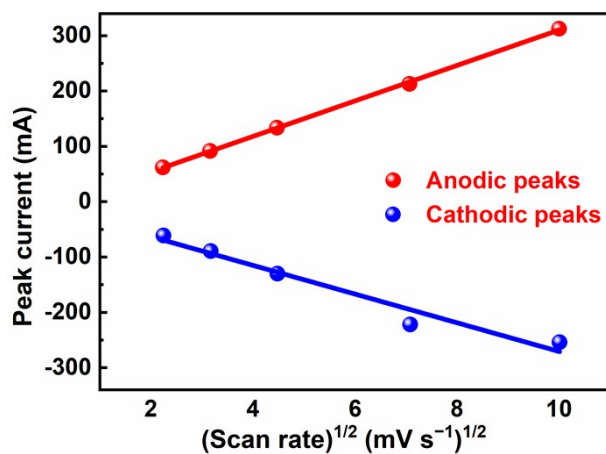

Fig. S8. The relationship between the scanning rate and peak current density of NiMOF/CNTs 180.

Table S1. Comparison of the performance of different electrodes under three electrode systems.

Electrode materials	Organic ligand	Specific capacity	Current density	Ref.
NiMOF/CNTs 180	2-methylimidazole	1855.0 F g^{-1}	1 A g^{-1}	This work
Cu-MOF/rGO	5-aminoisophthalic acid	867.1 F g^{-1}	1 A g^{-1}	[8]
Ni_xCo_{1-x} S/C	Trimesic acid	1575.6 F g^{-1}	1 A g^{-1}	[9]
ZnO/C@(Ni,Co)Se$_2$	2-methylimidazole	1477.0 F g^{-1}	1 A g^{-1}	[10]
Ni-Co LDH/Ti$_3$C$_2$T$_x$	2-methylimidazole	1271.4 F g^{-1}	1 A g^{-1}	[11]
NiP	Trimesic acid	1625.0 F g^{-1}	1 A g^{-1}	[12]
NiO/Ni-MOF	Terephthalic acid	1176.6 F g^{-1}	1 A g^{-1}	[13]
Ni_xCo_{1-x}Se$_2$/CNFs/CoO@CC	2-methylimidazole	1870.2 F g^{-1}	1 A g^{-1}	[14]
Cu$_9$S$_5$/C	Trimesic acid	1323.6 F g^{-1}	1 A g^{-1}	[15]
Ni-Zn hydroxide/rGO	2-methylimidazole	1538.5 F g^{-1}	1 A g^{-1}	[16]
Co-CH@Ni-MOFs	Terephthalic acid	1246.0 F g^{-1}	1 A g^{-1}	[17]
H-NiS$_{1-x}$/C	Trimesic acid	1728.0 F g^{-1}	1 A g^{-1}	[18]
Ni-MOF@Co(OH)$_2$	p-Phthalic acid	1448.0 F g^{-1}	2 A g^{-1}	[19]
HRGO/Ni(PA)$_2$	Picolinic acid	738.0 F g^{-1}	1 A g^{-1}	[20]
Ni(OH)$_2$/Co(OH)$_2$/Mg(OH)$_2$	2,5-dihydroxyterephthalic acid	1481.8 F g^{-1}	1 A g^{-1}	[21]
CNTs/Ni-Co LDH	Pure terephthalic acid	1628.0 F g^{-1}	1 A g^{-1}	[22]
CeO$_2$@(Ni, Co)$_3$S$_4$	Trimesic acid	1319.0 F g^{-1}	1 A g^{-1}	[23]
CNTs@Co-BTC	Trimesic acid	553.3 F g^{-1}	1 A g^{-1}	[24]

Table S2. Specific capacitance and Specific capacitance retention of NiMOF/CNTs 180 at different Current density.

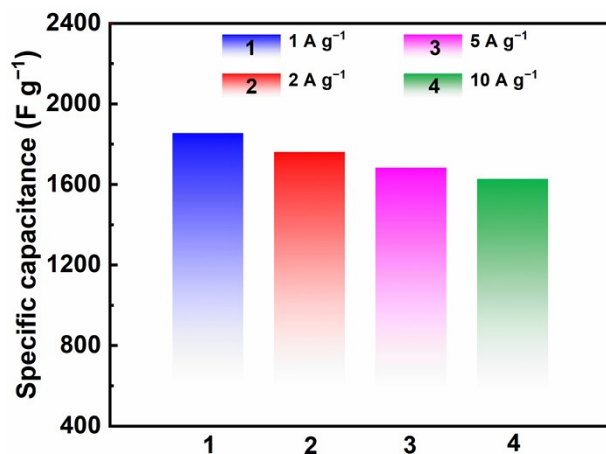| Current density (A g⁻¹)	Specific capacitance (F g⁻¹)	Specific capacitance retention (%)
1	1855	1
2	1761	94.9
5	1683	90.7
10	1626.9	87.7

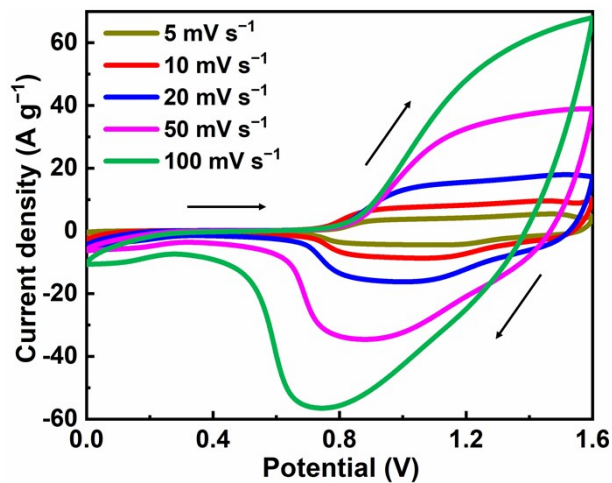**Fig. S9.** The specific capacitance of NiMOF/CNTs 180 at different current density.

Fig. S10. CV curves of NiMOF/CNTs 180//AC at various scanning rates.

Table S3. Energy density and power density of NiMOF/CNTs 180//AC and other previously reported devices.

Device	Energy density Wh kg^{-1}	Power density W kg^{-1}	Ref.
NiMOF/CNTs 180//AC	113.8	800.0	**This work**
AHPC// AHPC	107.0	900.0	[25]
NiO/NC-700 //NC	40.2	750.2	[26]
Zn H-ZHS//AC	286.6	220.0	[27]
N-rGO//N-rGO	55.0	1800.0	[28]
Zn H-ZHS//AC	190.3	89.8	[29]
Co$_{2-x}$Ni$_x$P-N-C-2//AC	86.0	800.0	[1]
CNG-900// CNG-900	92.0	1000.0	[30]
NiMn-Gly-1//AC	54.4	800.0	[31]
Co-Ni-S NPs/Cu-Ni-Mn-O //Mn-Zn-Fe-O/G-ink	75.6	6629.5	[32]
KF-CMNWs/Ni//M-CNTF	62.9	984.0	[33]

Table S4. The original dimensions of the commercial MWCNTs.

Material	Diameter distribution	Length	Surface area
MWCNTs	25-35 nm	15-30 μm	250-270 m^2 g^{-1}

As we can see (Fig. S11a), for freshly prepared NiMOF/CNTs 180 electrodes (before testing and cycling), the NiMOF nanosheets evenly distributed around the CNTs, and the small amount of film and nanoparticles in the electrodes might be polyvinylidene fluoride (PVDF) and conductive carbon (CC).[34, 35] As in Fig. S11b-d, the diameter (30-35 nm) of CNTs almost did not change significantly after different cycles of GCD test.
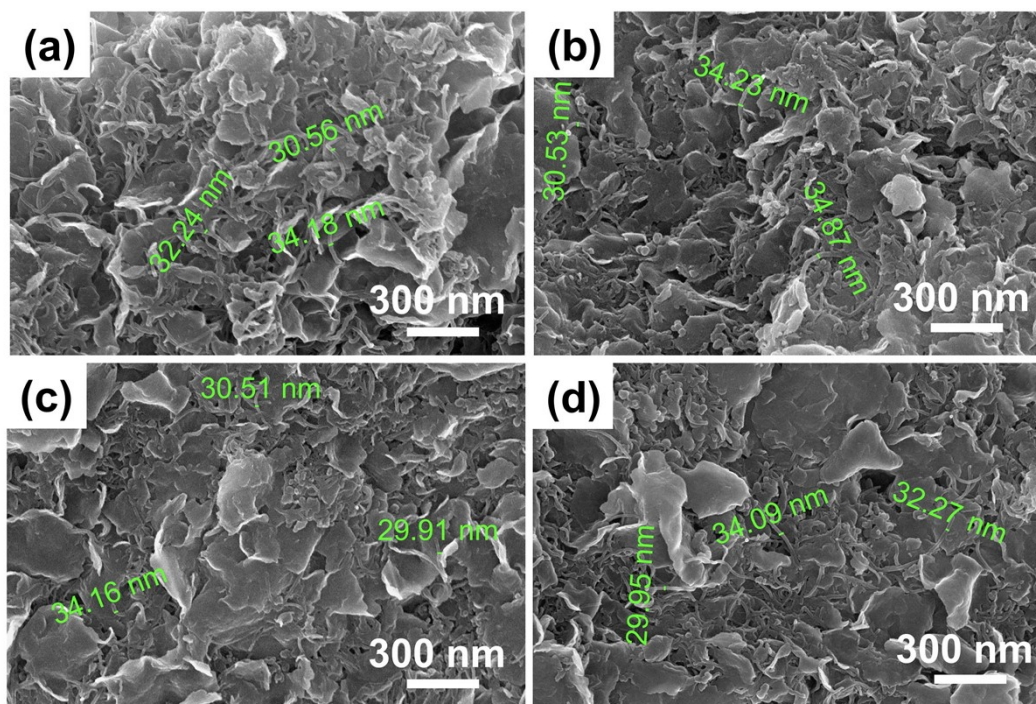

Fig. S11. SEM of the NiMOF/CNTs 180 electrodes with conductive agent and PVDF, (a) Before cycle of GCD test; (b) After 1000 cycles of GCD test; (c) After 3000 cycles of GCD test, and (d) After 5000 cycles of GCD test.

As in Fig. S12, the pure NiMOF (Fig. S12a) is yellow-green and the NiMOF/CNTs 160 (Fig. S12b), NiMOF/CNTs 180 (Fig. S12c) and NiMOF/CNTs 200 (Fig.S12d) are black. Therefore, we painted the NiMOF nanosheets yellow-green and the carbon nanotubes black.
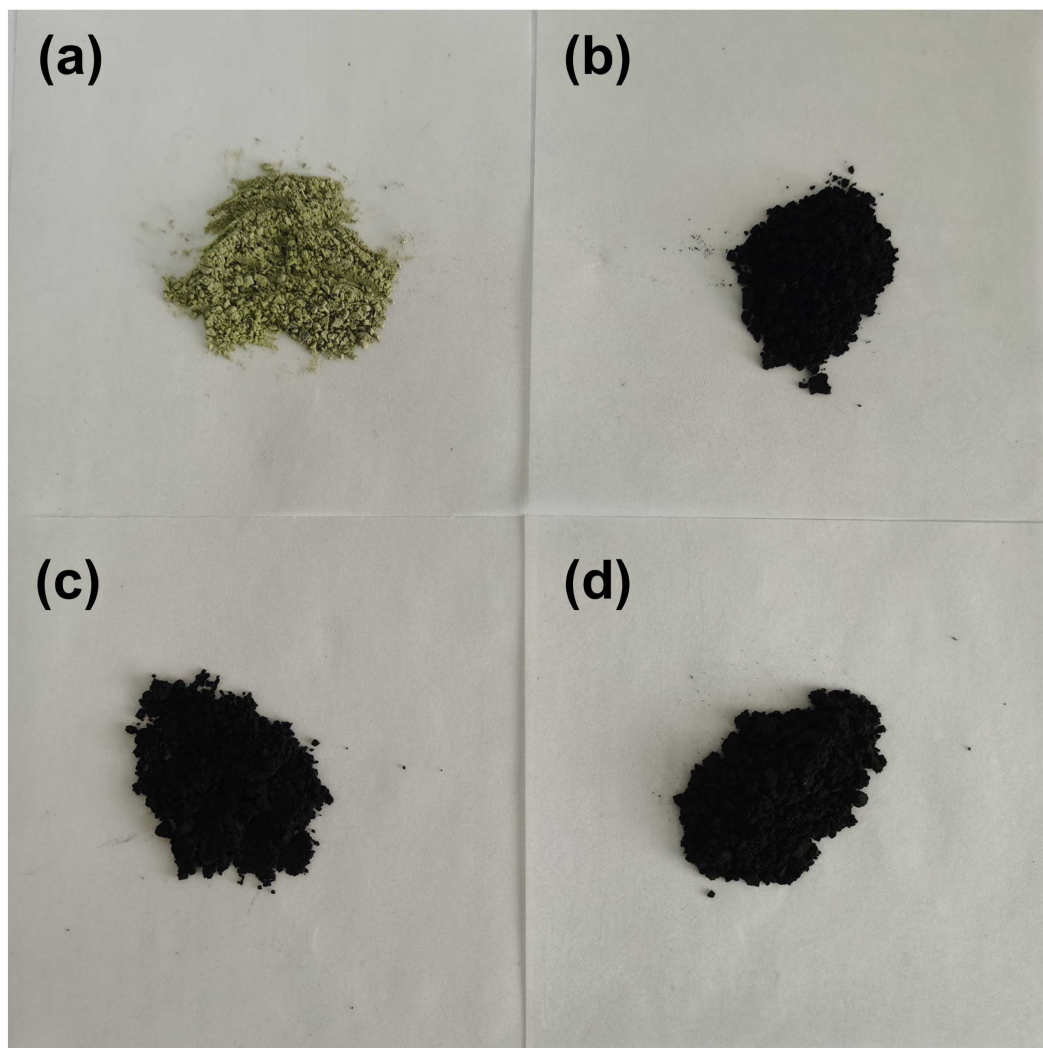

Fig. S12 (a) Photos of NiMOF 180; (b) NiMOF/CNTs 160; (c) NiMOF/CNTs 180; (d) NiMOF/CNTs 200.
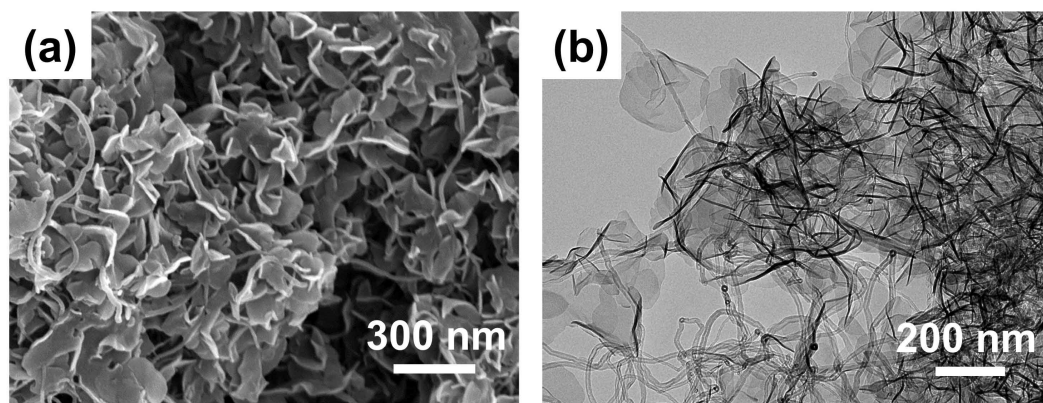
Fig. S13 (a-b) SEM and TEM images of NiMOF/CNTs 180.

Reference

1. L. Xu, Y. Xi, W. Li, Z. Hua, J. Peng, J. Hu, J.-J. Zhou, P. Zhang, J. Wang, W. Wang, H. Ding, W. Wang, W. Ji, Y. Yang, X. Xu, L. Chen and X. Li, *Nano Energy*, 2022, **91**, 106630.

2. S. S. Patil, J. C. Shin and P. S. Patil, *Ceram. Int.*, 2022, **48**, 29484-29492.

3. Q. Xu, Q.-X. Xie, T. Xue, G. Cheng, J.-D. Wu, L. Ning, X.-H. Yan, Y.-J. Lu, Z.-L. Zou, B.-P. Wang and F.-L. Han, *Chem. Eng. J.*, 2022, 451, 138775.

4. A. Ferse and B. Ferse, *Electrochim. Acta*, 2016, **192**, 497-511.

5. D.-H. Choi, Y. Li, G. R. Cutting and P. C. Searson, *Sens. Actuators B Chem.*, 2017, **250**, 673-678.

6. Y. Hoe Seon, Y. Chan Kang and J. S. Cho, *Chem. Eng. J.*, 2021, **425**, 129051.

7. L. Chai, Z. Hu, X. Wang, L. Zhang, T.-T. Li, Y. Hu, J. Pan, J. Qian and S. Huang, *Carbon*, 2021, **174**, 531-539.

8. S. Krishnan, A. K. Gupta, M. K. Singh, N. Guha and D. K. Rai, *Chem. Eng. J.*, 2022, **435**, 135042.

9. C. Huang, A. Gao, Z. Zhu, F. Yi, M. Wang, J. Hao, H. Cheng, J. Ling and D. Shu, *Electrochim. Acta*, 2022, **406**, 139872.

10. W. Liu, F. Zhu, B. Ge, L. Sun, Y. Liu and W. Shi, *Chem. Eng. J.*, 2022, **427**, 130788.

11. Y. Wang, C. Shi, Y. Chen, D. Li, G. Wu, C. Wang and L. Guo, *Electrochim. Acta*,

2021, **376**, 138040.

12. X. Ma, J. Chen, B. Yuan, Y. Li, L. Yu and W. Zhao, *Appl. Surf. Sci.*, 2022, **588**, 152928.

13. G. Wang, Z. Yan, N. Wang, M. Xiang and Z. Xu, *ACS Appl. Nano Mater.*, 2021, **4**, 9034-9043.

14. L. Sun, Y. Liu, M. Yan, Q. Yang, X. Liu and W. Shi, *Chem. Eng. J.*, 2022, **431**, 133472.

15. D. Xu, Y. Yang, K. Le, G. Wang, A. Ouyang, B. Li, W. Liu, L. Wu, Z. Wang, J. Liu and F. Wang, *Chem. Eng. J.*, 2021, **417**, 129350.

16. Y. Du, G. Li, L. Ye, C. Che, X. Yang and L. Zhao, *Chem. Eng. J.*, 2021, **417**, 129189.

17. X. Zhang, S. Yang, W. Lu, Y. Tian, Z. Liu, Y. Zhao and A. Liu, *Small*, 2022, **n/a**, 2200656.

18. C. Huang, A. Gao, F. Yi, Y. Wang, D. Shu, Y. Liang, Z. Zhu, J. Ling and J. Hao, *Chem. Eng. J.*, 2021, **419**, 129643.

19. X. Shi, T. Deng and G. Zhu, *J. Colloid Interface Sci.*, 2021, **593**, 214-221.

20. C. Yang, Q. Pan, Q. Jia, W. Qi, H. Wei, S. Yang, N. Hu and B. Cao, *Chem. Eng. J.*, 2021, **408**, 127302.

21. C. Hao, Y. Guo, W. Ren, X. Wang, L. Zhu, X. Wang and J. Wu, *Electrochim. Acta*, 2022, **412**, 140135.

22. M. Huang, Y. Wang, J. Chen, D. He, J. He and Y. Wang, *Electrochim. Acta*, 2021, **381**, 138289.

23. Z. Xue, C. Yang, K. Tao and L. Han, *Appl. Surf. Sci.*, 2022, **592**, 153231.

24. H. Zhang, Y. Sun, X. Zhang, H. Yang and B. Lin, *Electrochim. Acta*, 2021, **389**, 138684.

25. G. Zhao, C. Chen, D. Yu, L. Sun, C. Yang, H. Zhang, Y. Sun, F. Besenbacher and M. Yu, *Nano Energy*, 2018, **47**, 547-555.

26. C. Huang, S. Lv, A. Gao, J. Ling, F. Yi, J. Hao, M. Wang, Z. Luo and D. Shu, *Chem. Eng. J.*, 2022, **431**, 134083.

27. L. Han, H. Huang, X. Fu, J. Li, Z. Yang, X. Liu, L. Pan and M. Xu, *Chem. Eng. J.*,

2020, **392**, 123733.

28. S. Dai, Z. Liu, B. Zhao, J. Zeng, H. Hu, Q. Zhang, D. Chen, C. Qu, D. Dang and M. Liu, *J. Power Sources*, 2018, **387**, 43-48.

29. G. Yang, J. Huang, X. Wan, Y. Zhu, B. Liu, J. Wang, P. Hiralal, O. Fontaine, Y. Guo and H. Zhou, *Nano Energy*, 2021, **90**, 106500.

30. X. Xu, J. Yang, X. Zhou, S. Jiang, W. Chen and Z. Liu, *Chem. Eng. J.*, 2020, **397**, 125525.

31. S. Ding, J. An, D. Ding, Y. Zou and L. Zhao, *Chem. Eng. J.*, 2022, **431**, 134100.

32. C. V. V. M. Gopi, R. Vinodh, S. Sambasivam, I. M. Obaidat, S. Singh and H.-J. Kim, *Chem. Eng. J.*, 2020, **381**, 122640.

33. S.-W. Zhang, B.-S. Yin, X.-X. Liu, D.-M. Gu, H. Gong and Z.-B. Wang, *Nano Energy*, 2019, **59**, 41-49.

34. S. Manoharan, P. Pazhamalai, V. K. Mariappan, K. Murugesan, S. Subramanian, K. Krishnamoorthy and S.-J. Kim, *Nano Energy*, 2021, **83**, 105753.

35. N. Jayababu and D. Kim, *Nano Energy*, 2021, **82**, 105726.